Increase in spin Hall effect and influence of anomalous Nernst effect on spin Hall magnetoresistance in β-phase and α-phase $W_{100-x}Ta_x$/CoFeB systems

Yoshiaki Saito[1 *], Nobuki Tezuka[2, 3], Shoji Ikeda[1, 3, 4], Hideo Sato[1, 3-6] and Tetsuo Endoh[1, 3-7]

[1]Center for Innovative Integrated Electronic Systems, Tohoku University, Sendai 980-0845, Japan

[2]Department of Materials Science, Graduate School of Engineering, Tohoku University, Sendai 980-8579, Japan

[3]Center for Spintronics Research Network, Tohoku University, Sendai 980-8577, Japan

[4]Center for Spintronics Integrated Systems, Tohoku University, Sendai 980-8577, Japan

[5]Research Institute of Electrical Communication, Tohoku University, Sendai 980-8577, Japan

[6]Center for Science and Innovation in Spintronics (Core Research Cluster), Tohoku University, Sendai 980-8577, Japan

[7]Department of electrical Engineering, Graduate School of Engineering, Tohoku University, Sendai 980-8579, Japan

(Dated: February 15, 2019)

[*] E-mail address: ysaito@cies.tohoku.ac.jp

Abstract

We studied spin Hall effect in $W_{100-x}Ta_x$ with various Ta compositions for W-Ta alloy/CoFeB/MgO heterostructures by means of spin Hall magnetoresistance (SMR). We synthesized W-Ta alloys with both α-phase and β-phase by controlling sputtering condition. We found that, in both α-phase and β-phase W-Ta alloys, the amplitude in SMR signals increases by alloying W with Ta at certain *x*. The analysis based on the drift diffusion model reveals that the increase in SMR originates from an enhancement of the spin Hall angles θ_{SH}. Moreover, we observed the influence of anomalous Nernst effect on SMR for the high resistive W-Ta/CoFeB systems.

Current-induced spin-orbit torque (SOT) originating from the spin-Hall effect (SHE) in heavy metal/ferromagnet (HM/FM) systems has attracted attention due to their potential for application in the efficient manipulation of magnetization of nano magnets in SOT magnetoresistive random access memory (SOT-MRAM), skyrmion and domain wall devices. [1–16)] Materials as well as HM/FM interfaces with larger spin-orbit coupling have been attracting interest because they allow a larger amount of spin current (J_s) to be generated for manipulating the magnetization when the write charge current (J_C) is passed through the HM layers. Magnitudes of the spin-Hall angle ($\theta_{SH} = J_S/J_C$) have been determined for various HMs by measuring the spin-Hall magnetoresistance (SMR) and spin torque ferromagnetic resonance (ST-FMR) [17-21)] and by other means. W in which the crystalline structure is polycrystalline $A15$ (β-phase) or a mixture of β-phase and amorphous phase have large magnitudes of θ_{SH}. [1, 12, 17, 18, 21)] Due to the extensive efforts, the efficiency of present SOT operations, that is, the absolute values of θ_{SH} ($|\theta_{SH}|$) becomes larger day by day, however, almost all HMs with large magnitude of $|\theta_{SH}|$ have a very high resistivity (ρ_{xx}). For instance, β-W has a relatively large $|\theta_{SH}|$ of approximately 0.3, however has very high resistive (ρ_{xx} ≈200-300 $\mu\Omega$cm) [18, 21)]; $|\theta_{SH}|$ generally reported for Pt and β-Ta is approximately 0.1, and β-Ta is also very high resistive (ρ_{xx} ≈200 $\mu\Omega$cm). [1, 12, 21)] The low $|\theta_{SH}|$ and high ρ_{xx} lead to an undesirably large energy dissipation, delay in speed, and large voltage drop during current flow in HMs. These features are not desirable for an application to large scale integrations (LSIs). More recently, large magnitudes of $|\theta_{SH}|$ have also been observed in

transition metal compounds and topological insulators such as W-oxides [22], Cu-oxides, [23] and BiSb, [24] however, these materials have also very high ρ_{xx} of 150 - 300 $\mu\Omega$cm and $\sim 9\times10^3$ $\mu\Omega$cm, and $\sim$ 400 $\mu\Omega$cm, respectively.

For solving these issues, increasing the intrinsic SHE by band engineering is very important. The intrinsic spin Hall angle is given by

$$\theta_{SH} = \frac{J_S}{J_C} = \frac{e}{\hbar}\frac{\sigma^Z_{XY}}{\sigma_{XX}}, \qquad (1)$$

where e is the charge of an electron, $\hbar$ is Dirac constant, σ^Z_{XY} is transverse spin conductivity, σ_{XX} is longitudinal charge conductivity. Recent *ab initio* electronic structure calculation [25] has suggested that alloying W with Ta is particularly effective in increasing the absolute value of $|\sigma^Z_{XY}|$ for both crystalline structures of β-phase and α-phase.

Here, we report that experimental observation of the increase in SHE for $W_{100-x}Ta_x$ alloys with both β-phase and α-phase by investigating the SMR measurements. Because the resistivity of $W_{100-x}Ta_x$ slightly decreases with increasing Ta concentration in the case of β-phase $W_{100-x}Ta_x$ we prepared here, the observed increase in the magnitude of the $|\theta_{SH}|$ in the β-phase $W_{100-x}Ta_x$ would be related to the increase in an intrinsic SHE. [25] Moreover, we show the influence of the sample heating on spin Hall magnetoresistance especially for the high resistive HM/FM systems.

Film stacks Ta(0.5 nm)/W(t nm)/$Co_{20}Fe_{60}B_{20}$(1.5 nm)/MgO(1.5 nm)/Ta(1.0 nm) (Fig. 1(a)) and Ta(0.5 nm)/(W(0.32 nm)/Ta(y nm))$_n$/$Co_{20}Fe_{60}B_{20}$(1.5 nm)/MgO(1.5 nm)/Ta(1.0 nm) (y = 0.08, 0.16,

0.32, *n*: repetition number) (Fig. 1(b)) are deposited on a highly resistive Si substrate by rf magnetron sputtering. Base pressure of the sputtering system is less than 1.5×10^{-7} Pa. We prepared the samples with various W and W-Ta alloy film thicknesses for measurements of SMR between ~1.5 and ~7.0 nm. For the preparation of the W-Ta alloys, we used artificial synthesized method [26] and W one monolayer and less than one monolayer Ta were alternately grown at room temperature. The detailed HM structures are W (1.5～7 nm) (Samples No. 1 and 5), $(W(0.32\ nm)/Ta(0.08))_n$ (n=4～18) (Samples No. 2 and 6), $(W(0.32\ nm)/Ta(0.16))_n$ (n=3～15) (Samples No. 3 and 7) and $(W(0.32\ nm)/Ta(0.32))_n$ (n=2～11) (Samples No. 4 and 8). Ar gas pressure (P_{Ar}) during deposition of the W and W-Ta between the samples No. 1–4 (high-resistive-phase deposition condition) and 5–8 (low-resistive-phase deposition condition) are changed to P_{Ar}^{W}/P_{Ar}^{Ta} = 2.55 Pa/0.39 Pa and P_{Ar}^{W}/P_{Ar}^{Ta} = 0.39 Pa/0.13 Pa for changing the resistivity of the W and W-Ta alloys. The easy axis of the CoFeB layer with 1.5 nm thickness is confirmed to be in the film plane from vibrating sample magnetometer. We also confirmed that the dead layer thickness is ~0 nm for the CoFeB layer in all samples annealed at 300°C. For all films, the saturation magnetization (M_S) value of $Co_{20}Fe_{60}B_{20}$ is ~1500 emu/cm^3. This value is nearly consistent with the nominal $Co_{20}Fe_{60}B_{20}$ saturation magnetization. [27] After the deposition, the films are patterned into a microscale Hall bar by photolithography and Ar ion milling. After ion milling, immediately SiO_2 was deposited and lift-off. Finally, Ta (230 nm) electrodes are formed at the ends of the channel and Hall probes by photolithography and lift-off processes. The processed wafers are

annealed at 300°C for an hour. Figures 1(c) and 1(d) are the schematic diagram of the devices and the typical device photography, respectively. For the measurements of SMR, the current, which is less than equal to 6 μA, is passed through the devices in the *x-axis* direction in Fig. 1(c) and external magnetic field between -4 and +4 Tesla is applied to the both y- and z-axes directions by using the Quantum Design, Physical Properties Measurement System at 305 K.

Figures 1(e) and 1(f) are the results of x-ray diffraction (XRD) measurements for the stacks with thicknesses of W and W-Ta alloys: t ~7 nm. A standard Cu anode x-ray tube operated at 45 kV accelerating voltage and 200 mA filament current was used to generate x-rays. The magnitude of the intensity for the out-of-plane XRD θ - 2θ diffraction patterns for the stacks deposited at high-resistive-phase condition is less than half of those deposited at low-resistive-phase condition, and the peak intensity for the stack with W deposited at high-resistive-phase condition is very small and broad in the width as shown in Fig. 1(e). The observed broad out-of-plane XRD θ - 2θ diffraction pattern for W indicates the HM films deposited at high-resistive-phase condition contain an amorphous phase and observed narrow peak patterns for W-Ta alloys are originated from α-phase (bcc) W-Ta (110). As shown in Figs. 1(e) and 1(f), the peak position of 2θ decreases with increasing Ta concentration x monotonically in $W_{100-x}Ta_x$ alloys. This indicates lattice constant of W-Ta increases with increase of Ta concentration and artificial synthesized (W (0.32 nm)/Ta(y nm))$_n$ multilayers form W-Ta alloys. Therefore, from here, we call (W (0.32 nm)/Ta(y nm))$_n$ multilayers (y = 0.08, 0.16, 0.32) $W_{100-x}Ta_x$ (x

= 25, 33, 50 at. %) alloys, respectively, for the convenience. The inset of Fig. 1(e) shows the in-plane XRD $2\theta_{\chi}$–φ diffraction pattern for the sample No.1 with high-resistive-phase W condition and t =7 nm. The peak positions for the stacks are related to the β-phase W (200), (210) and (211) peak positions. Therefore, the high-resistive-phase stacks would contain both amorphous and β-phase $W_{100-x}Ta_x$.

Figures 2 (a) and 2(b) show the inverse of the device longitudinal resistance ($1/R_{xx}$) multiplied by a geometrical factor (L/w), the sheet conductance, $G_{xx} = L/(wR_{xx})$ values are plotted as a function of the HM layer thickness (t) for the sample No.1-4 prepared at high-resistive-phase condition and the sample No.5-8 prepared at low-resistive-phase condition, respectively, where L = 205 μm and w = 5.8 μm as shown in Fig. 1(c). As shown in Fig. 2(a), there is no anomaly for the device with high-resistive W, whereas there are phase transition from mixture of amorphous and β-phase to α-phase W-Ta for the device with high-resistive $W_{75}Ta_{25}$, $W_{67}Ta_{33}$ and $W_{50}Ta_{50}$ alloys at the phase transition thickness: t_T = 4.92, 3.37 and 2.74 nm, respectively. The t_T is thinner for the stacks prepared at low Ar gas sputtering process as shown in Fig. 2(b) (t_T = 3.08, 2.65, 2.67 and 2.44 nm for W, $W_{75}Ta_{25}$, $W_{67}Ta_{33}$ and $W_{50}Ta_{50}$, respectively). Therefore, we used the samples No. 1-4 for analyzing the data of SMR for estimating the absolute values of θ_{SH} and spin diffusion length (λ_S) in the mixture of amorphous and β-phase $W_{100-x}Ta_x$, and the samples No. 5-8 for estimating those in the α-phase $W_{100-x}Ta_x$ alloys. The values of the resistivity ($\rho_{W\text{-}Ta}$) for the mixture of amorphous and β-phase $W_{100-x}Ta_x$ alloys, α-phase $W_{100-x}Ta_x$ alloys are shown in inset in Fig. 2(a). The obtained value of the resistivity (ρ_{CoFeB}) for $Co_{20}Fe_{60}B_{20}$ is

ρ_{CoFeB} = 139.9 $\mu\Omega$cm. The estimated resistivity values of β-phase W, α-phase W, and CoFeB are consistent with previous reports. [17, 18, 21)]

Figures 3(a) and 3(b) show the typical R_{xx} versus external magnetic field (H) measured at 305 K for the devices with W (Sample No. 1) and for that with $W_{67}Ta_{33}$ alloys (Sample No. 3), respectively. As shown in Figs. 3(a) and 3(b), the values of longitudinal resistance R_{xx} in the magnetic field directions along z-axis: $H_z > 0$ T and $H_z < 0$ T are nearly same (for example, R_{xx} (H_z = 4 T) ～ R_{xx} (H_z = -4 T)), however, the values of R_{xx} in the magnetic field directions along y-axis: $H_y > 0$ T and $H_y < 0$ T are different from each other for the both devices with W and $W_{67}Ta_{33}$ alloys. For the devices with W, the value of R_{xx} at H_y = 4 T is smaller than that at H_y = -4 T, and for the devices with W-Ta alloys, the value of R_{xx} at H_y = 4 T is larger than that at H_y = -4 T as shown in Figs. 3(a) and 3(b). These are related to the anomalous Nernst voltage due to the thermal hot electron current flow from the film to substrate. We will discuss the detail in later. In order to neglect the thermal effect to analyze the SMR, we define the SMR by

$$SMR = \Delta R_{XX}/R_{XX}^{H=0} = [\Delta R_{XX}^{1} + \Delta R_{XX}^{2}]/2R_{XX}^{H=0}, \quad (2)$$

$$\Delta R_{XX}^{1} = R_{XX}(H_y = -1.6\ \mathrm{T}) - R_{XX}(H_Z = -1.6\ \mathrm{T}), \quad (3)$$

$$\Delta R_{XX}^{2} = R_{XX}(H_y = +1.6\ \mathrm{T}) - R_{XX}(H_Z = +1.6\ \mathrm{T}), \quad (4)$$

where $R_{XX}^{H=0}$ is the longitudinal resistance at H = 0 T. Because we consider that the slight increase in ΔR_{XX} with increasing $|H|$ above 1.6 T may originate from contribution of the Hanle magnetoresistance, [28, 29)] which causes an increase in R_{XX} ($|H_Z| \geq 1.6$ T) with increasing $|H|$ and enhancement of ΔR_{XX}. Therefore, we used the values of R_{XX} at $|H|$ = 1.6 T, which is the saturation magnetic field value for

CoFeB in the magnetic hard-axis direction, for the estimation of SMR.

Next, we evaluated the θ_{SH} and λs in the HM electrode for samples No. 1-4 and 5-8 by using SMR. Figures 3(c) and 3(d) show the $\Delta R_{XX}/R_{XX}^{H=0}$ as a function of t and $t' = t - t_T$ for samples No. 1-4 and No. 5-8, respectively. The solid lines in Figs. 3(c) and 3(d) are the results fitted the measured data by the following equations: [17, 21)]

$$\mathrm{SMR} = \Delta R_{XX}/R_{XX}^{H=0} \sim \theta_{SH}^2 \frac{\lambda_S}{t} \frac{\tanh(t/2\lambda_S)}{1+\xi} \left[1 - \frac{1}{\cosh(t/\lambda_S)}\right], \quad (5)$$

$$\xi \equiv \frac{\rho_{W-Ta} t_{CoFeB}}{\rho_{CoFeB} t}, \quad (6)$$

where t_{CoFeB} is the thickness of the ferromagnetic layer of CoFeB. This applied SMR model is based on the drift diffusion model, [30)] therefore the estimated θ_{SH} and the λs are all effective values. The magnitudes of $|\theta_{SH}|$ and λs of the W-Ta HM electrodes are successfully obtained.

Figures 4(a) and 4(b) show the results of the magnitudes of $|\theta_{SH}|$ and λs as a function of the Ta concentration (x) in $W_{100-x}Ta_x$. The values of θ_{SH} and λs are -0.20, -0.21, -0.20, -0.19 and 1.05 nm, 1.09 nm, 0.81 nm, 0.63 nm, for the devices with β-phase W, $W_{75}Ta_{25}$, $W_{67}Ta_{33}$ and $W_{50}Ta_{50}$, respectively. The values of θ_{SH} and λs are -0.07, -0.10, -0.11, -0.10 and 0.45 nm, 0.49 nm, 0.50 nm, 0.43 nm, for the devices with α-phase W, $W_{75}Ta_{25}$, $W_{67}Ta_{33}$ and $W_{50}Ta_{50}$, respectively. The values of θ_{SH} and λs in W is consistent with the previous report. [21)] We found that the magnitude of $|\theta_{SH}|$ for the devices with β-phase $W_{100-x}Ta_x$ alloys has a maximum around $x \sim 25$ as shown in Fig. 4(a), even though the resistivity of β-phase $W_{100-x}Ta_x$ alloys decreases with increasing Ta concentration as shown

in inset in Fig. 2 (a). Therefore, observed maximum around $x \sim 25$ for $|\theta_{SH}|$ would be related to the increase in intrinsic SHE as predicted by the theory. [25] Surprisingly, the magnitude of $|\theta_{SH}|$ for α-phase $W_{100-x}Ta_x$ alloys is nearly same with that of β-phase Ta as shown in Fig. 4(a), and that for α-phase $W_{100-x}Ta_x$ alloys has a maximum around $x \sim 33$, even though the resistivity values of α-phase $W_{100-x}Ta_x$ alloys are about 13% (see inset of Fig. 2(a)) of that of β-phase Ta. [1, 12] Our experimentally obtained features of the θ_{SH} for β- and α-phases $W_{100-x}Ta_x$ alloys shown in Fig. 4(a) are consistent with the theoretical calculation [25] of σ_{XY}^{Z} for both β- and α-phases W, taking into account the rigid-band model. We also find that the λs shown in Fig. 4(b) for β-phase $W_{100-x}Ta_x$ alloys suddenly decreases at $x>25$, whereas that for α-phase $W_{100-x}Ta_x$ alloys is nearly constant between $0 \leq x \leq 50$. The value of λs for β-phase $W_{50}Ta_{50}$ alloy is nearly same with that of β-phase Ta. [16, 21] The sudden change in λs for β-phase $W_{100-x}Ta_x$ alloys might be related to the structural change from β-phase W structure (*A*15) to β-phase Ta structure (tetragonal *P*42/mnm).

Finally, we would like to discuss the reason for the difference between the values of R_{xx} at magnetic field $H_y > 0$ T and those at $H_y < 0$ T for the both devices with W and W-Ta alloys shown in Figs. 3(a) and 3(b). Figure 5(a) shows $\Delta V_{XX} = I\Delta R_{XX} = I(R_{XX}(H_y = 4\ \mathrm{T}) - R_{XX}(H_y = -4\ \mathrm{T}))$ as a function of $I\,(R_{XX}^{H=0})^2$ for all samples we prepared (Samples No. 1-8), where I is the current values during the measurements of SMR at 305 K. When $I\,(R_{XX}^{H=0})^2 \gtrsim 0.024\ \ \Omega^2\mathrm{A}$, the values of ΔV_{XX} monotonically decrease and increase with increase of $I\,(R_{XX}^{H=0})^2$ for the devices with W HM and for those with W-Ta

alloy HM, respectively. When the $I\,(R_{XX}^{H=0})^2 \gtrsim 0.024\ \Omega^2$A, that is, the resistance of the film R_{XX} is large, a temperature gradient ($-\nabla T$) should form between the film and substrate as shown in Figs. 5(b) and 5(c). This induces the hot electron flow ($-j_h$) from the film to the substrate. In this situation, when H_y is applied and the magnetization of CoFeB is pointing along +y and -y, anomalous Nernst voltage due to the thermal hot electron flow should be observed as shown in Figs. 5(b) and 5(c). This indicates that in the case of the films with high resistive HM, the influence of anomalous Nernst voltage should be considered for obtaining the correct values of θ_{SH} and λs. There are other thermal effects, for example, the longitudinal spin Seebeck effect [31] and spin-dependent Seebeck effect [32]. Especially, the device structure is a little bit resemble in the case of the longitudinal spin Seebeck effect. [31] However, the spin Seebeck effect can be detected by means of the inverse spin hall effect (ISHE), so, voltage contact connects directly with a heavy metal. In our case, voltage contact connects directly with ferromagnetic metal (CoFeB). Moreover, in Ref. 31), for observing longitudinal spin Seebeck effect, a ferromagnetic insulator was used in order to increase the ISHE signal. When ferromagnetic metal is used (our case) as the ferromagnetic layer, the ISHE signal is suppressed significantly by short-circuit currents in the ferromagnetic layer due to the electric conduction of ferromagnet and an anomalous Nernst signal amplitude would increase largely. Therefore the main reason for the thermal effect we observed would be related to the anomalous Nernst effect.

In order to secure the thermal effect in SMR, we prepare the devices changing the stacking order

between CoFeB and W or CoFeB and W-Ta and with same thickness of W and W-Ta as the devices shown in Figs. 3 (a) and (b). Changing the stacking order from the devices (samples No. 1–8), the thermal flow into the CoFeB would be increased because the heating source is W or W-Ta layers. As a result, we observed increase in the asymmetry ($\Delta R_{XX}^{H//y}$) for R_{xx} vs H curves for H//y-axis direction. This indicates the increase in thermal effect. Thus, we can get another evidence of the thermal effect in SMR.

Figures 3(a), 3(b) and 4(a) show that the current flow direction of J_C^{Nernst} originating from the anomalous Nernst voltage is different from each other between the devices with W HM and W-Ta HM as shown in Figs. 5(b) and 5(c). When there is a temperature difference ΔT between a film and substrate, the anomalous Nernst voltage is expressed as [33)]

$$\Delta V_{XX}/\Delta T \propto \frac{\xi}{1+\xi}(\theta_{\mathrm{AH}}S - \theta_{\mathrm{AN}}S_{\mathrm{F}}) - \frac{1}{1+\xi}(\theta_{\mathrm{SH}}(\theta_{\mathrm{SH}}S - \theta_{\mathrm{SN}}S_{\mathrm{N}})\frac{\lambda_{\mathrm{S}}}{t}\tanh\left(\frac{t}{2\lambda_{\mathrm{S}}}\right) Im\left[\frac{g_{\mathrm{S}}}{1+g_{\mathrm{S}}\cosh\left(\frac{t}{\lambda_{\mathrm{S}}}\right)}\right], \quad (7)$$

where θ_{AH} is the anomalous Hall angle of CoFeB, θ_{AN} is the anomalous Nernst angle of CoFeB, S_{F} is the Seebeck coefficient of CoFeB, θ_{SN} is the spin Nernst angle of HM layer, S_{N} is the Seebeck coefficient of HM layer, S is the Seebeck coefficient of HM/CoFeB bilayers defined by $S=(\xi S_{\mathrm{F}} + S_{\mathrm{N}})/(1+\xi)$, and $g_{\mathrm{S}} = 2\rho\lambda_{\mathrm{S}}G_{\mathrm{MIX}}$, where G_{MIX} is the spin-mixing conductance of the HM/CoFeB interface. There are three possibilities for the reason of the sign change in ΔV_{XX} between the films with W HM and W-Ta HM. The first is the case that the signs of S_{F} and S_{N} are different from each other and the magnitude of S_{N} largely changes for the addition of Ta in $W_{100-x}Ta_x$/CoFeB. The second

is case that both the θ_{SH} and second term in Eq. (7) are large and the sign of the imaginary part of spin-mixing conductance: $Im\left[\frac{g_S}{1+g_S\cosh\left(\frac{t}{\lambda s}\right)}\right]$ changes for the addition of Ta in $W_{100-x}Ta_x$/CoFeB. The third is the case that the mixing CoFeB with W-Ta HM is large and the sign of θ_{AN} changes for this mixing. As described in Ref. 33), because the signs of the imaginary part of spin-mixing conductance for both W and Ta are negative, therefore, the case 2 would be not the reason for explaining our data. As described before, the magnetic dead layers of CoFeB for all devices are nearly zero and the M_s is nearly consistent with the nominal CoFeB saturation magnetization. Therefore, these indicate that the third case is not the reason for explaining our data. Therefore, the first case would be more reasonable reason for explaining our data. However, more experimental efforts would be necessary to conclude the reason of the sign change in the anomalous Nernst voltage for addition of Ta in $W_{100-x}Ta_x$/CoFeB.

In conclusions, we studied the detailed SMR measurements for $W_{100-x}Ta_x$/CoFeB system and experimentally found that the alloying of $W_{100-x}Ta_x$ with both β-phase and α-phase structures increases spin Hall angles, comparing with those of β-phase and α-phase W, respectively. This would be related to the increase in intrinsic SHE. Moreover, we observed the influence of the anomalous Nernst voltage on spin Hall magnetoresistance. In a high resistive HM/FM system, in order to obtain correct magnitudes of θ_{SH} and λs, an influence of the sample heating should be taking into account.

ACKNOWLEDGEMENTS

The authors thank S. Sugimoto for various supports and developing research environments. The authors also thank M. Hayashi for useful discussion about the reason for the sign change in anomalous Nernst voltage, and K. Kataoka for technical support for the experiments. This work was partly supported by the Open Innovation Platform with Enterprises, Research Institute and Academia (OPERA), JST, and JSPS KAKENHI Grant Number 15H05699 and 19H00844.

REFERENCES

1) L. Liu, C.-F. Pai, Y. Li, H. W. Tseng, D. C. Ralph, and R. A. Buhrman, Science **336**, 555 (2012).

2) G. Yu, P. Upadhyaya, Y. Fan, J. G. Alzate, W. Jiang, K. L. Wong, S. Takei, S. A. Bender, L.-T. Chang, Y. Jiang, M. Lang, J. Tang, Y. Wang, Y. Tserkovnyak, P. K. Amiri, and K. L. Wang, Nat. Nanotechnol. **9**, 548 (2014).

3) W. Jiang, P. Upadhyaya, W. Zhang, G. Yu, M. B. Jungfleisch, F. Y. Fradin, J. E. Pearson, Y. Tserkovnyak, K. L. Wang, O. Heinonen, S. G. E. Velthuis, and A. Hoffmann, Science **349**, 283 (2015).

4) P. P. J. Haazen, E. Mure, J. H. Franken, R. Lavrijsen, H. J. M. Swagten, and B. Koopmans, Nat. Mater. **12**, 299 (2013).

5) A. Chernyshov, M. Overby, X. Liu, J. K. Furdyna, Y. Lyanda-Geller, and L. P. Rokhinson, Nat. Phys. **5**, 656 (2009).

6) I. M. Miron, K. Garello, G. Gaudin, P. –J. Zermatten, M. V. Costache, S. Auffret, S. Bandiera, B. Rodmacq, A. Schuhl, and P. Gambardella, Nature **476**, 189 (2011).

7) J. Kim, J. Sinha, M. Hayashi, M. Yamanouchi, S. Fukami, T. Suzuki, S. Mitani, and H. Ohno, Nat. Mater. **12**, 240 (2013).

8) S. Fukami, T. Anekawa, C. Zhang, and H. Ohno, Nat. Nanotechnol. **11**, 621 (2016).

9) K. –S. Lee, S. –W. Lee, B. –C. Min, and K. –J. Lee, Appl. Phys. Lett. **104**, 072413 (2014).

10) K. Garello, C. O. Avci, I. M. Miron, M. Baumgartner, A. Ghosh, S. Auffret, O. Boulle, G. Gaudin, and P. Gambardella, Appl. Phys. Lett. **105**, 212402 (2014).

11) C. Zhang, S. Fukami, H. Sato, F. Matsukura, and H. Ohno, Appl. Phys. Lett. **107**, 012401 (2015).

12) M. –H. Nguyen, C. –F. Pai, K. X. Nguyen, D. A. Muller, D. C. Ralph, and R. A. Buhrman, Appl. Phys. Lett. **106**, 222402 (2015).

13) S. Fukami, T. Anekawa, C. Zhang, and H. Ohno, Nat. Nanotechnol. **10**, 1038 (2016).

14) S. V. Aradhya, G. E. Rowlands, J. Oh, D. C. Ralph, and R. A. Buhrman, Nano Lett. **16**, 5987 (2016).

15) M. Baumgartner, K. Garello, J. Mendil, C. O. Avci, E. Grimaldi, C. Murer, J. Feng, M. Gabureac, C. Stamm, Y. Acremann, S. Finizio, S. Wintz, J. Raabe, and P. Gambardella, Nanotechnol. **12**, 980 (2017).

16) Y. Kato, Y. Saito, H. Yoda, T. Inokuchi, S. Shirotori, N. Shimomura, S. Oikawa, A. Tiwari, M. Ishikawa, M. Shimizu, B. Altansargai, H. Sugiyama, K. Koi, Y. Ohsawa, and A. Kurobe, Phys. Rev. Appl. **10**, 044011 (2018).

17) J. Liu, T. Ohkubo, S. Mitani, K. Hono, and M. Hayashi, Appl. Phys. Lett. **107**, 232408 (2015).

18) C. –F. Pai, L. Liu, Y. Li, H. W. Tseng, D. C. Ralph, and R. A. Buhrman, Appl. Phys. Lett. **101**, 122404 (2012).

19) A. Ganguly, K. Kondou, H. Sukegawa, S. Mitani, S. Kasai, Y. Niimi, Y. Otani, and A. Barman, Appl. Phys. Lett. **104**, 072405 (2014).

20) Y. Wang, P. Deorani, X. Qiu, J. H. Kwon, and H. Yang, Appl. Phys. Lett. **105**, 152412 (2014).

21) J. Kim, P. Sheng, S. Takahashi, S. Mitani and M. Hayashi, Phys. Rev. Lett. **116**, 097201 (2016).

22) K. –U. Demasius, T. Phung, W. Zhang, B. P. Hughes, S. –H. Yang, A. Kellock, W. Han, A. Pushp, and S. Parkin, Nat. Commun. **7**, 10644 (2016).

23) H. An, Y. Kageyama, Y. Kanno, N. Enishi, and K. Ando, Nat. Commun. **7**, 13069 (2016).

24) N. H. D. Khang, Y. Ueda, P. N. Hai, Nature Mater. **17**, 808 (2018).

25) X. Sui, C. Wang, J. Kim, J. Wang, S. H. Ehim, W. Duan and N. Kioussis, Phys. Rev. B **96**, 241105(R) (2017).

26) T. Kojima, M. Mizuguchi, T. Koganezawa, K. Osaka, M. Kotsugi and K. Takanashi, Jpn. J. Appl. Phys. **51**, 010204 (2012).

27) R. M. Bozorth, Ferromagnetism (Wiley-IEEE Press, New York, 1993).

28) M. I. Dyakonov, Phys. Rev. Lett. **99**, 126601 (2007).

29) S. Velez, V. N. Golovach, A. Bedoya-Pinto, M. Isasa, E. Sagasta, M. Abadia, C. Rogero, L. E. Hueso, F. S. Bergeret, and F. Casanova, Phys. Rev. Lett. **116**, 016603 (2016).

30) V. P. Amin and M. D. Stiles, Phys. Rev. B **94**, 104420 (2016).

31) K.Uchida, H. Adachi, T. Ota, H. Nakayama, S. Maekawa, E. Saitoh, Appl. Phys. Lett. 97, 172505 (2010).

32) F. K. Dejene, J. Flipse, B. J. van Wees, Phys. Rev. B. 86, 024436 (2012).

33) P. Sheng, Y. Sakuraba, Y. –C. Lau, S. Takahashi, S. Mitani, M. Hayashi, Science Adv. **3**, e1701503 (2017).

Figure captions

Fig. 1 Cross-section view of the sputtered film stacks for (a) W/CoFeB system and (b) W-Ta/CoFeB system. (c) Schematic diagram and (d) a photograph of a prepared device. (e), (d) are results of the out-of-plane x-ray diffraction (XRD) θ–2θ diffraction patterns for the stacks with 7 nm thicknesses of W and W-Ta alloys prepared by (e) high-resistive-Ar-pressure condition (Sample No. 1-4) and (d) low-resistive-Ar-pressure condition (Sample No. 5-8). Inset of (e) is the in-plane XRD $2\theta_\chi$–φ diffraction pattern for the stack with 7 nm thickness of W prepared by high-resistive-Ar-pressure condition (Sample No. 1).

Fig. 2 Sheet conductance (G_{xx}) as a function of W-Ta thickness (t) for the devices prepared by (a) high-resistive-Ar-pressure condition (Sample No. 1-4) and (b) low-resistive-Ar-pressure condition (Sample No. 1). The solid lines in (a) and (b) are linear fits to the data. Inset in (a) is the resistivity (ρ_{W-Ta}) of $W_{100-x}Ta_x$ HM as a function of Ta concentration x.

Fig. 3 Typical longitudinal resistance R_{xx} versus external magnetic field H oriented along the y axis (red circles) and z axis (black circles) measured at 305 K for (a) the device with 2.5 nm W (Sample No. 1) and for (b) the device with 2.4 nm $W_{67}Ta_{33}$ alloy (Sample No. 3). SMR $\Delta R_{XX}/R_{XX}^{H=0}$ plotted against the HM layer thickness t for (c) Sample No. 1-4 with β-phase $W_{100-x}Ta_x$ HM and (d) the SMR

plotted against $t' = t - t_T$ for Sample No. 5-6 with α-phase $W_{100-x}Ta_x$ HM. The solid lines show the fitting results using drift diffusion model. [17, 21]

Fig. 4 (a) Estimated magnitude of the Spin Hall angle $|\theta_{SH}|$ and (b) spin diffusion length λ_S as a function of Ta concentration x in the $W_{100-x}Ta_x$ alloys for the devices with β-phase $W_{100-x}Ta_x$ HM (black squares and black triangles, respectively) and for those with α-phase $W_{100-x}Ta_x$ HM (red squares and red triangles, respectively). Black and red solid lines in (a), (b) are guides for the eyes.

Fig. 5 (a) Difference of the voltages $\Delta V_{XX} = I\Delta R_{XX}$ between H = -4 T and 4 T as a function of I $(R_{XX}^{H=0})^2$ for all samples we prepared (Samples No. 1-8). (b), (c) are schematic diagrams for explaining the reason of the ΔV_{XX} by an anomalous Nernst voltage.

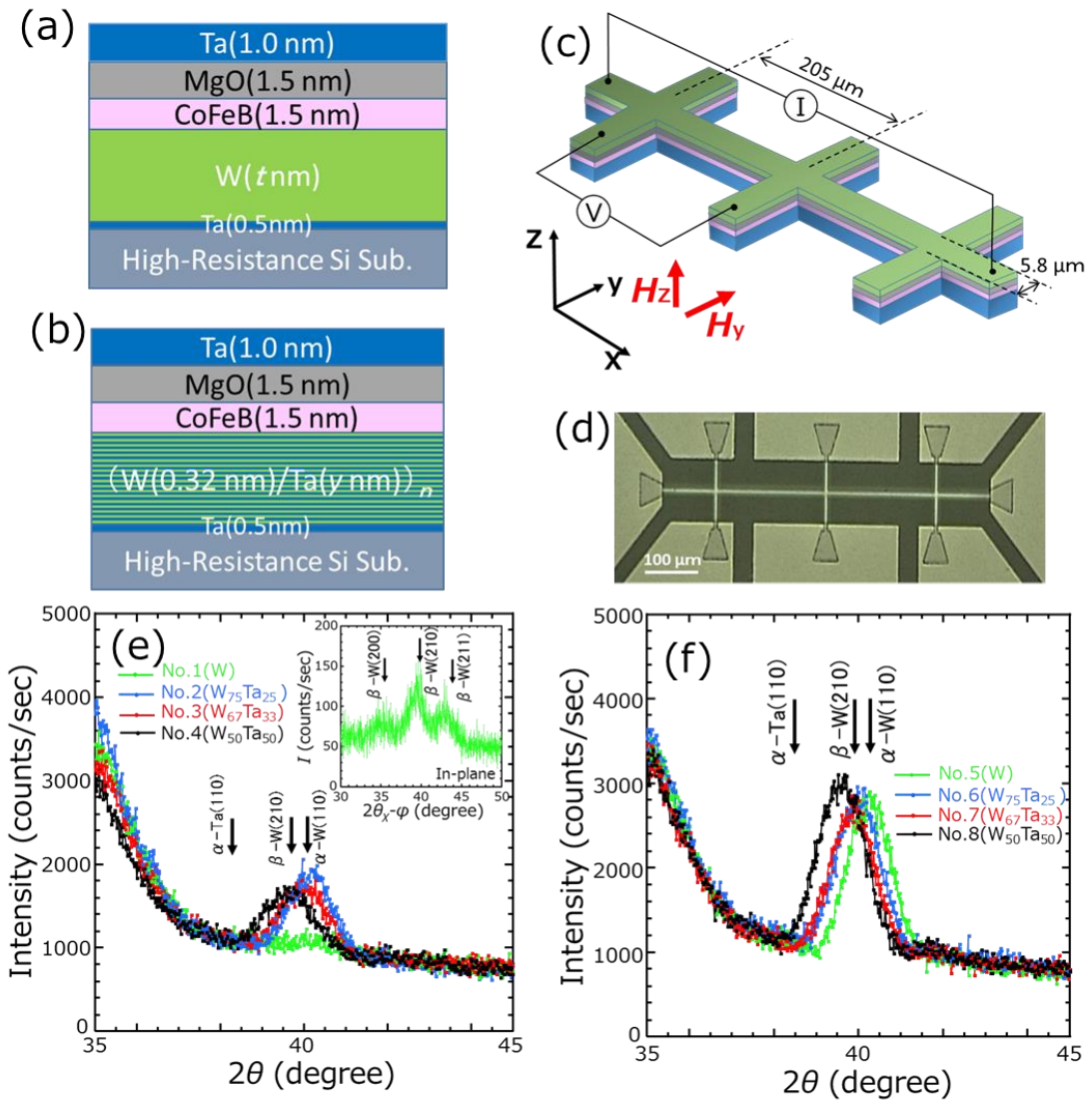

Fig. 1 Y. Saito et al.

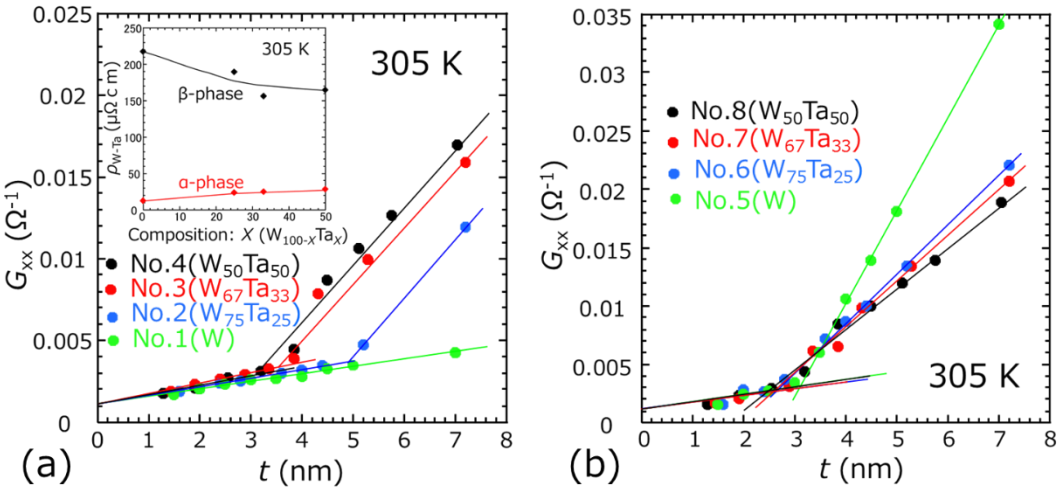

Fig. 2 Y. Saito et al.

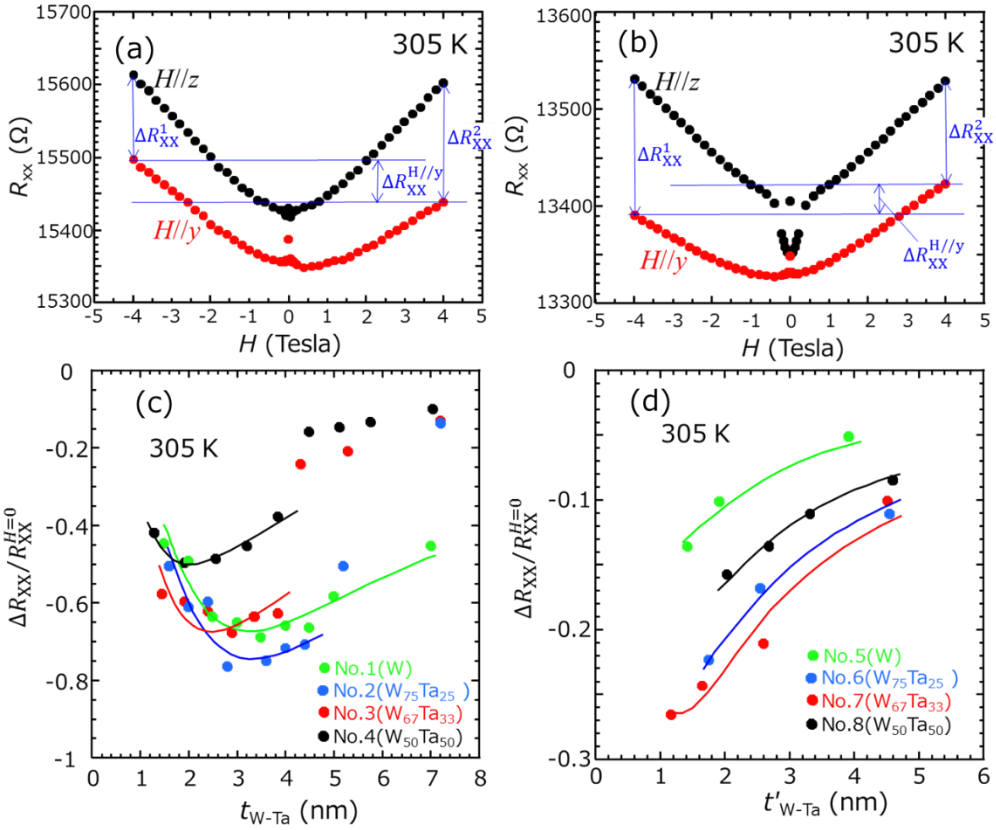

Fig. 3 Y. Saito et al.

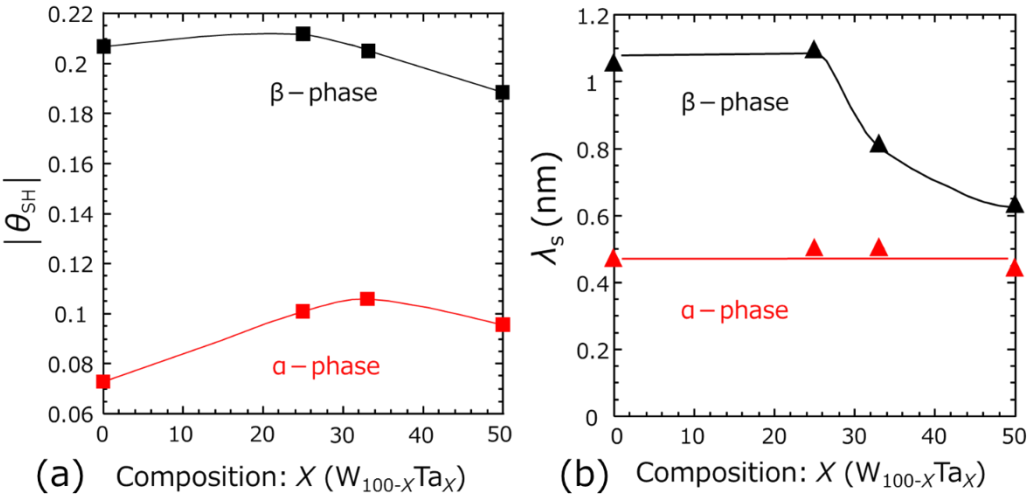

Fig. 4 Y. Saito et al.

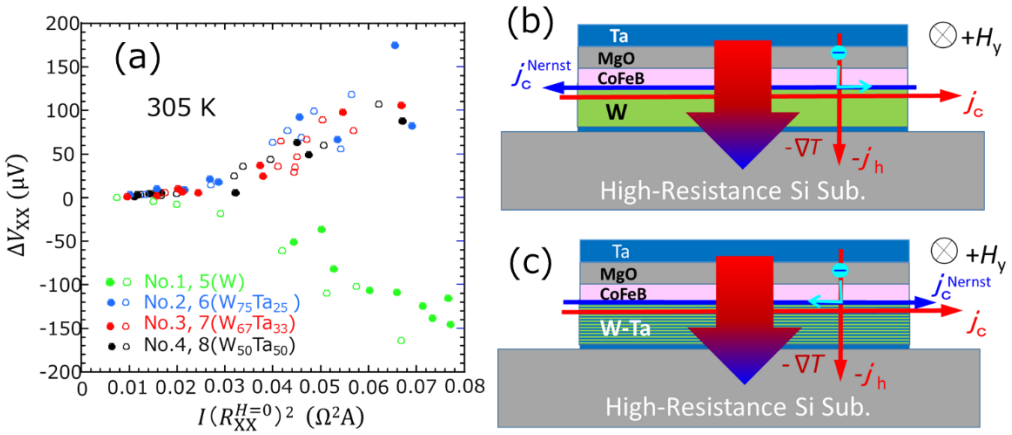

Fig. 5 Y. Saito et al.